Observing Relative Homotopic Degeneracy Conversions with Circuit Metamaterials

Maopeng Wu,[1,*] Mingze Weng,[1,*] Zhonghai Chi,[1] Yingyi Qi,[1] Hui Li,[1] Qian Zhao,[1,†] Yonggang Meng,[1] and Ji Zhou[2]

[1]*State Key Laboratory of Tribology in Advanced Equipment, Department of Mechanical Engineering, Tsinghua University, Beijing 100084, China*

[2]*State Key Laboratory of New Ceramics and Fine Processing, School of Materials Science and Engineering, Tsinghua University, Beijing 100084, China*

(Received 28 March 2023; accepted 4 December 2023; published 5 January 2024)

Making nodal lines (NLs) deterministic is quite challenging because directly probing them requires bulk momentum resolution. Here, based on the general scattering theory, we show that the Bloch modes of the circuit metamaterials can be selectively excited with a proper source. Consequently, the transport measurement for characterizing the circuit band structure is momentum resolved. Facilitated by this bulk resolution, we systematically demonstrate the degeneracy conversions ruled by the relative homotopy, including the conversions between Weyl points (WPs) and NLs, and between NLs. It is experimentally shown that two WPs with opposite chirality in a two-band model surprisingly convert into an NL rather than annihilating. And the multiband anomaly (due to the delicate property) in the NL-to-NL conversions is also observed, which in fact is captured by the non-Abelian relative homotopy. Additionally, the physical effects owing to the conversions, like the Fermi arc connecting NLs and the parallel transport of eigenstates, are discussed as well. Other types of degeneracy conversions, such as those induced by spin-orbit coupling or symmetry breaking, are directly amenable to the proposed circuit platform.

DOI: 10.1103/PhysRevLett.132.016605

Introduction.—In three dimensions (3D), robust band degeneracies in semimetals can manifest as discrete points or closed lines. In the case of degeneracy points, there are Weyl points (WPs) and Dirac points [1]. Weyl and Dirac semimetals have attracted considerable attention owing to their characteristic topological surfaces [2] and novel responses to applied external fields [3,4]. On the other hand, nodal lines (NLs) [5–7], in the form of closed lines, require additional symmetry by contrast (such as *PT* symmetry). They may behave as various shapes in the Brillouin zone (BZ), such as rings [8,9], chains [10–12], knots [13–15], and links [16–19]. Interestingly, degeneracies can mutually convert. For example, an NL breaks into Weyl or Dirac points as a result of spin-orbit coupling or symmetry breaking [7,20–23], a nodal ring converts into a nodal chain due to the topological transition [10–12,24–26].

Recently, homotopy theory has been applied to understand the band intersection, which includes the complete nodal classification [27] and the degeneracy conversions [5,28]. Beyond the established "tenfold way" methods, one of the unique generalizations from the homotopy description is the non-Abelian nodal-line semimetals [5,29], which feature braiding topological structures [30–32] and trajectory-dependent node transfers [33–37]. However, those predicted conversions in 3D have not been observed.

It seems that directly characterizing the band degeneracies of 3D semimetals is impossible. Experimentally, the angle-resolved transmission spectroscopy (ARPES, e.g., [11,38,39]) and the Fourier-transformed field scan (FTFS, e.g., [19,33]) are the primary approaches to measure the band structures. But, neither of them is applicable because the former has limited momentum resolution in the perpendicular direction [7], and field distributions in the latter are hardly accessible in 3D. The topological signature on the surface can reduce the 3D measurement task to a 2D one. For example, the Fermi arc of the boundary modes always terminates at WPs [2], so instead of directly measuring WPs, one can characterize the Fermi arc first through 2D ARPES or FTFS [40,41] and extract WPs from the arc. The same procedure can be applied to those NLs with drumhead surface states [8]. But NL semimetals normally do not have topologically protected boundary modes [1,7,42], e.g., the NLs considered here.

Another challenge is the metamaterialization of semimetals. The tight-binding approximation is widely adopted to describe the band structure in the theory of semimetals [1] and topological insulators [43]. But localized orbits are not desired bases for optics [44], and adding the model-required terms, such as the long-range hopping, is extremely difficult (even impossible). The site-resolved topological circuits [45–49] may provide a manageable platform since the circuit network has a one-to-one correspondence to a tight-binding model and the required terms are possible to realize. But, the existing circuits are experimentally unfeasible in observing degeneracy conversions [50].

Here, based on the temporal topolectrical circuits (TTCs) proposed previously [54], we show that the selective excitation enables us to acquire the band information along with the specific crystal orientation, leaving the TTCs bulk momentum resolved. We experimentally show that a pair of WPs related by the mirror symmetry can convert into an NL, and this annihilating anomaly is topologically obstructed by the relative homotopy. As for NL-to-NL conversions, we demonstrate that the multiband generalization of the non-Abelian homotopic description precisely controls these conversions.

Momentum-resolved circuits.—We first briefly review the TTCs. The admittance of the circuit in a lattice structure can be written as $\mathbf{J}(w,\mathbf{k}) = Y\mathbf{I} + \mathbf{J}_0(w,\mathbf{k})$, where $Y\mathbf{I}$ is the so-called self-admittance and preset to be identical. Tuning $Y\mathbf{I}$ globally will offset the eigenvalues of the admittance, and it doesn't cause any physical effect since it can be gauged out. But for TTCs, it controls the eigenvectors $\mathbf{V}_{\mathbf{k},0}$ without changing the operating frequency [54]. Compared to the existing topolectrical circuits [45,46], this feature greatly facilitates the band characterization since it can be achieved by generic transport or scattering measurements [50] [e.g., Fig. 1(b)].

The TTCs are bulk momentum resolved, which is critical to observing NLs, if the Bloch modes in the circuit metamaterials can be selectively excited. The coupling rate between the field ψ in a source and the Bloch mode $\boldsymbol{\phi}_\mathbf{k}$ determines how well the mode is excited, and it is proportional to the overlap integral $\int d\mathbf{r}\psi^* \boldsymbol{\phi}_\mathbf{k}$. The vanishing coupling indicates that the mode cannot be excited by the source even $\psi \neq 0$. So, roughly analogous to the phase array antenna, we can selectively excite the modes through a properly configured source. The idea for the proof is briefly outlined below with more details given in the Supplemental Material (SM) [50].

Assuming that N ports are connected to the internal sites of the lattice at $\mathbf{r}_i$ [Fig. 1(a)]. Employing $i = 1, \ldots, N-1$ as sources and $i = N$ as a receiver, we now calculate the transmission T between them. Given the coupling matrix $\mathbf{w}$ between the sites and ports, the excited states $\mathbf{u}$ in the lattice is

$$\mathbf{u} = G\sum_i [\mathbf{w\Psi}]_i, \qquad G = (E - \mathbf{H})^{-1}, \tag{1}$$

where $\mathbf{H}$ is the Hamiltonian and $\mathbf{\Psi}$ is the state vector of ports. Now consider a line source [blue line in Fig. 1(a)]. The excitations are arranged to be the same as one eigenstate $|l\rangle$ of $\mathbf{H}$ up to constant times c_0: $[\mathbf{w\Psi}]_n = c_0[|l\rangle]_{\mathbf{r}_i}$. Then $\mathbf{u} = G|\mathbf{k_0}\rangle\delta_{\mathbf{r},\mathbf{r}_i}$, which follows from the fact that the eigenstates in the real and momentum spaces are related by $|\mathbf{k_0}\rangle = \sum e^{i\mathbf{k}_0\cdot\mathbf{r}}|l\rangle$. Using the general expression [55,56] for scattering, we have the transmission (see SM [50])

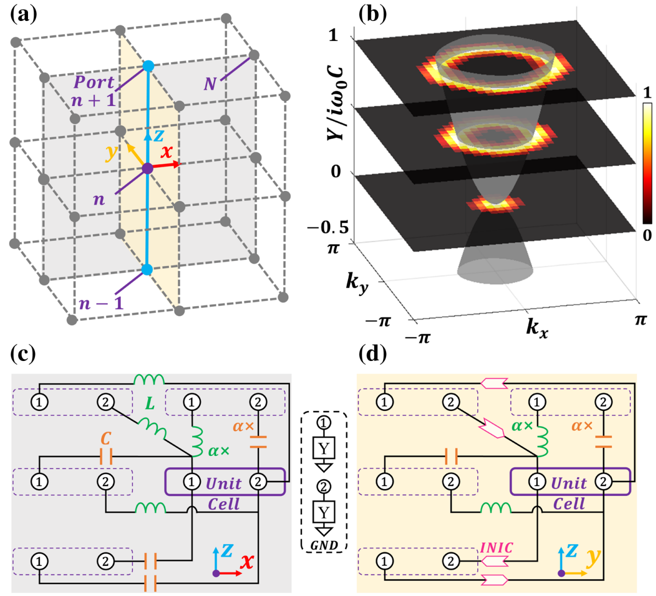

FIG. 1. Momentum-resolved TTCs due to the selective excitation and the Y-enabled FTFS. (a) The line source consisting of $N-1$ ports (blue line) would excite the Bloch states with momentum $\mathbf{k_0}$, while the port N is used to receive the signal. The transmission between line source and port N is formulated by Eq. (2). (b) Quadratic degeneracy formed by the Weyl node colliding [with respect to the inset of Fig. 2(b)]. The planes with scaled colors show the Fourier-transformed field distribution (FTFD) from experiments. Note that FTFD corresponds to the isoenergy (or iso-self-admittances) contour. (c) and (d) The circuit realization of J_1 in (x,z) and (y,z), respectively. $L = 30$ uH, $C = 10$ nF, and $\alpha\times$ denotes α components in parallel. The self admittances are preset to be Y. For more details see SM [50].

$$T(\mathbf{r}_N) \propto \sum_{\mathbf{k}_0} \frac{|\mathbf{k_0}\rangle\langle\mathbf{k_0}|}{E - E(\mathbf{k}_0) + i\Gamma}, \tag{2}$$

where Γ is the port self-energy and $E(\mathbf{k}_0)$ is the eigenvalue with respect to $|\mathbf{k_0}\rangle$. The above can be extended to the circuit by noting the corresponding $\mathbf{H} \leftrightarrow \mathbf{J}, E \leftrightarrow Y$. The transmission for characterizing the band *only* depends on the Bloch states with momentum $\mathbf{k_0}$, so the TTCs are momentum resolved. For experimental simplicity, all the models considered here are finely tuned such that the excitation ports have no phase difference.

Two types of models with mirror symmetry m_z along z are considered: (i) a model without global symmetries (e.g., time-reversal T), to demonstrate the WP-to-NL conversions; therein T breaking allows for the existence of WPs; (ii) the PT-symmetric models (space-inversion P) that exhibit the NL-to-NL conversions, where the PT symmetry implies NL degeneracies. All conversions mentioned above are ruled by the relative homotopy.

WP-to-NL conversions.—Without loss of generality, we consider the minimal model with two bands [the circuit realization, see Figs. 1(c) and 1(d)]:

$$(jw_0C)^{-1}J_1(\mathbf{k}) = 2\sin k_z(\sin k_x\sigma_x + \sin k_y\sigma_y) - [-1.5 + \cos k_x + \cos k_y - \alpha\cos k_z]\sigma_z \tag{3}$$

where $\boldsymbol{\sigma}$ are the Pauli matrices and α is the tuning parameter. J_1 is m_z symmetric: $\sigma_z J_1(\mathbf{k}_\perp, k_z)\sigma_z = J_1(\mathbf{k}_\perp, -k_z)$ with σ_z being its representation and $\mathbf{k}_\perp = (k_x, k_y)$. Breaking the T symmetry, which is achieved by current negative impedance converter (INIC) components here, may be extremely difficult for other platforms.

The evolution of the two opposite WPs in this model is anomalous beyond the widely held paradigm. To show that, we first set $\alpha = 1$ such that our model has two m_z-related WPs with opposite chirality [Figs. 2(a) and 2(d)]. Two WPs will move toward each other when α decreases until $\alpha = 0.5$. In that case, two WPs will collide on the m_z-symmetric plane $\Pi = (\mathbf{k}_\perp, 0/\pi)$ [Figs. 2(b) and 2(e)], forming a double Weyl node which does not have a linear dispersion in all directions [33] [inset of Figs. 2(b) and 1(b)]. According to a widely held paradigm [1], the two WPs will annihilate when $\alpha < 0.5$, because topological charge $n = +1 - 1 = 0$ on a sphere that encloses both WPs. Here, we set the chirality of the red WP in Fig. 2 to $+1$, while the black WP is set to -1. However, the expected annihilation does not happen, instead, two points convert into an NL [Figs. 2(c) and 2(f)].

This anomaly can be well explained by the relative homotopic description $\pi_2(M_2, X_m)$ of degeneracies. M_2 is the ensemble of all possible gapped 2-by-2 Hermitian matrices [e.g., $J_1(\mathbf{k})$], and $X_m \subset M_2$ commutates with σ_z for $\forall\ \mathbf{k} \in \Pi$. To calculate the topological charge n_r of $\pi_2(M_2, X_m)$, one needs to specify a symmetric sphere (just like the sphere surrounding WPs mentioned above). However, half of the sphere with its equator lying on Π [e.g., the blue hemisphere D^2 in Fig. 2(a)] is sufficient since it is identical to the upper half of the sphere and fully contains the topological information. The nontrivial n_r corresponds to the WP-to-NL conversion [28] (n_r also known as the delicate Chern number [58]). Here, $\pi_2(M_2, X_m) = \mathbb{Z}$ (integer group) and $n_r = 1$ on D^2, implying the conversion. To show that, supposing the WPs can vanish by tuning α, one can gap out the WPs by annihilation, so that there is no singularity inside D^2, contradicting the assumption that $n_r = 1$. In this sense, the annihilation of the WPs is obstructed by $n_r = 1$ on D^2.

The conversion indicator n_r also suggests the chiral Fermi arc on the surface [Figs. 2(g) and 2(h)]. The argument for the presence of the Fermi arc is similar to that of WPs [2,28] (note that $n_r = 1$ on D^2 is equal to n on a sphere that solely includes the red WP), and the arc terminates at the critical points of conversion. Besides, like the usual mirror-protected NLs, the model of J_1 also has drumhead surface states [Fig. 2(i)] bounded by the NL projection onto the surface Brillouin zone [Figs. 2(g) and 2(i)]. Those surface states may help to measure the degeneracies, but the exhibition of surface states is not universal (e.g., J_2 and J_3).

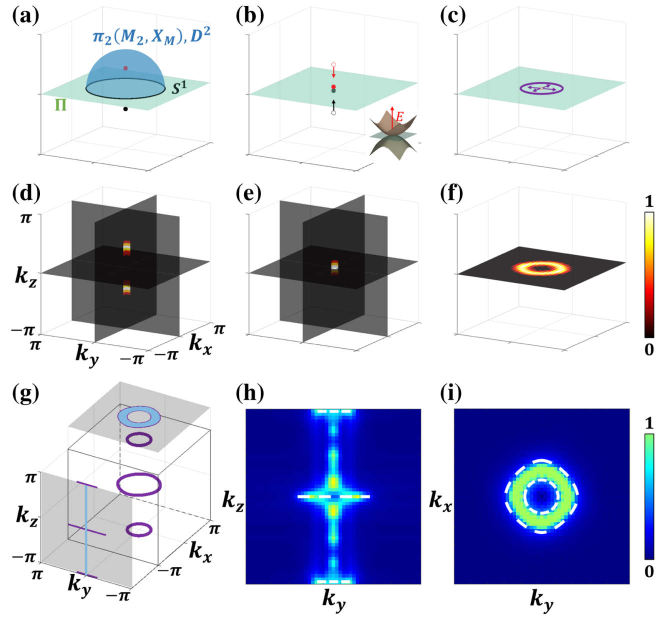

FIG. 2. Weyl point conversion determined by the relative homotopy group $\pi_2(M_2, X_M)$. The green plane denotes the m_z-invariant plane Π. (a) m_z-related WPs with opposite chirality. The blue hemisphere is the embedding D^2 used in $\pi_2(M_2, X_M)$, and $D^2 \cap \Pi = S^1$ (black ring) which is a constant in M_2 (i.e., D^2 is closed in M_2). So, n_r on D^2 is equal to n on a sphere that solely includes the red WP: $n_r = 1$. $\alpha = 1$. (b) WPs colliding on Π form a quadratic degeneracy (inset). $\alpha = 0.5$. (c) WPs convert to an NL (purple circle) rather than annihilating. $\alpha = 0$. We do not plot the NL on the $k_z = \pi$ plane for clarity since it can be evaded by the selective excitation. (d)–(f) FTFD in BZ with respect to (a)–(c) from experiments. The face and line current sources are used to excite the degeneracy modes in (a), (b), and (c), respectively. The voltage distribution in the real space recorded by an oscilloscope is mapped into the BZ via the Fourier transform. (g) NL projection and isoenergy contour of surface states on the surface BZ (grey plane). Fermi arc (blue line) and drumhead states (blue annulus) are supported by J_1 simultaneously. (h), (i) FTFD of the Fermi arc and drumhead states in the surface BZ from simulation [57]. The white dashed line denotes the NL projection. We place a point source at the center of the metamaterial surface to maximally excite the surface modes.

NL to NL: Disentangling of CPs.—The NLs and the nontrivially converted NLs always intersect at crossing points (CPs). So, one can alternatively understand that $\pi_1(M, X_m)$ protects the CPs (SM [50]). Here, we first focus on the fact that the relative homotopy description established in two bands is absent due to the delicate property.

The next subsection will demonstrate the finer relative homotopic rules modified by the additional band.

The concrete circuit lattice model is

$$\frac{1}{2}(jw_0C)^{-1}J_2(\mathbf{k}) = (\cos k_x - 1)\lambda_4 + (\cos k_z - 1)\lambda_6 + \lambda_3 \cos k_y - \left(\sqrt{3}\lambda_8 - I\right)\frac{\alpha}{3}, \tag{4}$$

where λ_i is the Gell-Mann matrices. The above model does not respect m_z symmetry, but the $\mathbf{k}\cdot\mathbf{p}$ expression $J_2'(\mathbf{k})$ of $J_2(\mathbf{k})$ around $\mathbf{k_0} = (0, \pm\pi/2, 0)$ does, namely, $m_z J_2'(\boldsymbol{\kappa}_\perp, \kappa_z) m_z = J_2'(\boldsymbol{\kappa}_\perp, -\kappa_z)$ with $m_z = \mathrm{diag}(1, -1, 1)$ and $\boldsymbol{\kappa} = \mathbf{k_0} - \mathbf{k}$ (referred as emergent symmetry [58]). $J_2'(\mathbf{k})$ contains all the topological information, so we use $J_2'(\mathbf{k})$ to identify $\pi_1(M_{1,2}, X_m)$, but our discussion returns to $J_2(\mathbf{k})$ when working out the NL configurations. $\pi_1(M_{1,2}, X_m)$ is incapable of stabilizing CPs, implying the relative homotopic description is absent [5], where $M_{1,2}$ is the topological space of all distinct gapped PT-symmetric matrices and the subscript 1,2 implies that the occupied band and the upper two bands are considered separately.

The above absence is experimentally demonstrated as the following. First, we set $\alpha = 0.5$. The NLs of the lower two bands of J_2 take the form of the red lines in Fig. 3(a). Those red NLs intersect at CPs (indicated by red arrows). The red CPs survive until $\alpha = 0$ [Fig. 3(b)]. However, tuning α to negative values results in a separation of those red NLs [Fig. 3(c)]. Therefore, the red CPs are not stable. Such CP disentangling is impossible in two-band models (for more mathematical explanation see SM [50]). The above analysis neglects the blue NLs formed by the upper two bands because those two are considered as a single trivial band.

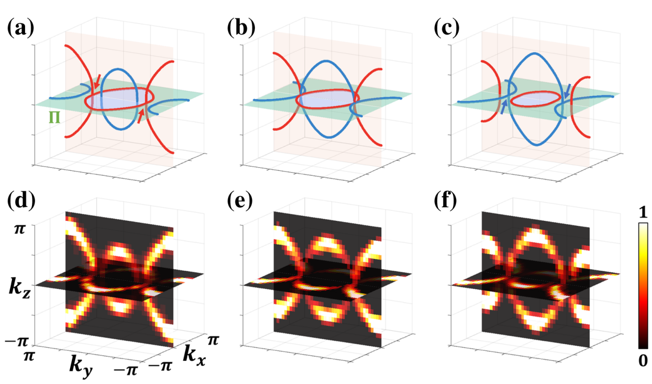

FIG. 3. The relative homotopy group $\pi_1(M_{1,2}, X_m)$ protecting red CPs is absent, and CP transfer for the three-band model. The red and blue lines denote the NLs formed by the lower and upper two bands, respectively. (a) Red CPs (indicated by red arrows) intersected by red NLs. $\alpha = 0.5$. (b) Red CPs survive when $\alpha = 0$. (c) Red CPs disentangle. $\alpha = -0.5$. Such CP disentangling is impossible in two-band models. In fact, red CPs transfer to blue CPs. (d)–(f) FTFD in the BZ with respect to (a)–(c) from experiments. A line source is used.

NL to NL: Non-Abelian entangling.—The non-Abelian NL braiding constrained by $\pi_1(M_3)$ has been shown experimentally in Refs. [30,31]. Here, we demonstrate the NL-to-NL conversions controlled by non-Abelian relative homotopy $\pi_1(M_3, X_m)$, which has not been experimentally reported elsewhere. Explicitly, the circuit model reads

$$\frac{1}{2}(jw_0C)^{-1}J_3(\mathbf{k}) = (\cos k_x - 1)\lambda_4 + (\cos k_z - 1)\lambda_6 + \left[\cos(2k_y) + \frac{\alpha}{2}\right]\frac{3\lambda_3 + \sqrt{3}\lambda_8 + 2I}{6} - \left(\sqrt{3}\lambda_8 - I\right)\frac{\cos k_y}{3}. \tag{5}$$

Similarly, the $\mathbf{k}\cdot\mathbf{p}$ expression J_3' has emergent m_z symmetry near $\mathbf{k_0} = (0, \pm\pi/2, 0)$. The model has extended and detangled NLs when $\alpha = 3$ [Figs. 4(a) and 4(e)]. NLs of different types stay extended until $\alpha = 2$, and they touch each other when $\alpha = 2$ [Figs. 4(b) and 4(f)]. However, further tuning $\alpha < 2$ does not force NLs to move across each other. In fact, they present as tangled NLs with an earring structure [$\alpha = 0$, Figs. 4(c) and 4(g)]. The long-range term may not be conveniently realized with other platforms.

The entangling of the model is consistent with the non-Abelian $\pi_1(M_3, X_m)$ with M_3 being the topological space of all distinct gapped 3-by-3 PT-symmetric matrices (e.g., $J_3'(\mathbf{k}) \subset M_3$). Compared to the relative homotopy mentioned above, the group elements herein are cosets. For example, the entangling in Fig. 4(g) is controlled by $\pi_1(M_3, X_m) = \{\{\pm 1, \pm j\}, \{\pm i, \pm k\}\}$, and $\{\pm i, \pm k\}$ is the nontrivial indicator of stabilizing CPs. The elements $\pm i$ and $\pm k$ correspond to loops that encircle NLs formed by the upper and lower two bands, respectively, while j encircles both, and the sign $\pm$ corresponds to the NL orientation. The elements in the coset are no longer integers since $\pi_1(M_3, X_m)$ partially inherits from $\pi_1(M_3)$, and they suggest that there are some uncertainties to be clear, e.g., the endpoints $\partial\gamma$ of γ in m_z-invariant plane Π, γ is the half loop to calculate the topological charge of $\pi_1(M_3, X_m)$. In Fig. 4(g), $\partial\gamma$ can be brought together along the orange circle. If we move $\partial\gamma$ such that they meet at A, the quaternion charge carried by γ is $\pm k$ since γ encloses a red NL. Similarly, γ carries $\pm i$ when they meet at B. This is consistent with the nontrivial coset $\{\pm i, \pm k\}$ that protects the CP (for more details see SM [50]).

The conversion also leads to the parallel transport effect of the eigenstates. Figure 4(h) shows the eigenstates evolve on γ with $\partial\gamma$ meeting at A. The red trace (eigenstates of the first band) and the orange trace (the second) change sign, while the blue one (the third) is unchanged. That means the eigenstates experience a rotation instead of just returning to initial states along the closed path γ. This is caused by the degeneracy of $\pm k$ ($\pm$ is differed by the orientation of

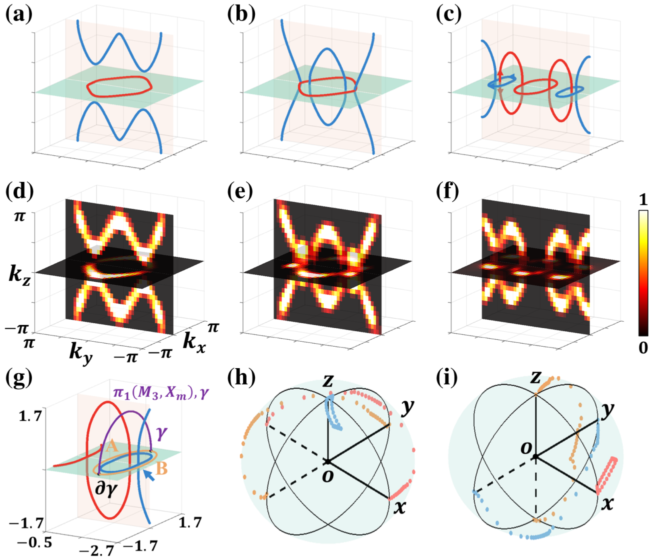

FIG. 4. CPs protected by the non-Abelian relative homotopy $\pi_1(M_3, X_m)$ and parallel transport of eigenstates due to the conversion. (a) Detangled and extended NLs. $\alpha = 3$. (b) NLs of different types move towards each other when $\alpha < 3$, and touch each other when $\alpha = 2$. (c) NLs do not cross each other and behave as the earring NLs. $\alpha = 0$. (d)–(f) FTFD in the BZ with respect to (a)–(c) from experiments. A line source is used. (g) Enlarged view of (c) to demonstrate the *CP* (indicated by the blue arrow) protected by the $\pi_1(M_3, X_m)$. Reconnecting $\partial\gamma$ at A or B on the orange circle corresponds to the nontrivial coset $\{\pm i, \pm k\}$ of $\pi_1(M_3, X_m)$. (h) Parallel transport on γ with two endpoints $\partial\gamma$ at A (from simulation [57]). The red, orange, and blue traces represent the eigenvectors of the first, second, and third bands, respectively. They are orthogonal and normalized, so we plot them on a sphere with the starting points. This continuous transport corresponds to $\pm k$. (i) Parallel transport on γ with two endpoints $\partial\gamma$ at B, This transport corresponds to $\pm i$. Above transport effects indicate the nontrivial coset $\{\pm i, \pm k\}$ that protects the *CP*. For more simulation details see SM [50].

the loop). A similar effect happens in Fig. 4(i), but the difference is that only the red trace returns back now since γ with $\partial\gamma$ at B surrounds $\pm i$. We remark that the observation of parallel transport is enabled by the momentum resolution of the proposed circuits.

Conclusion.—Directly evidencing the topological property in three dimensions that does not feature surface states is quite challenging. Here, we propose site-resolved and momentum-resolved circuits, which can serve as a general experimental platform. As an example of that, we experimentally demonstrate the band degeneracy conversions in semimetals. Our circuits may inspire metamaterial reverse design (such as that in acoustic [59] and electromagnetic [60] frequency range) since those can be simplified as the lumped parameter electrical circuits.

The authors thank Tomáš Bzdušek, Lei Kang, Fuli Zhang, Yuancheng Fan, Nianhai Shen, and Peng Zhang for useful discussions. In particular, we appreciate the review comments from Tomáš Bzdušek for helping us finish the manuscript. This work is supported by the National Key Research & Development Program of China (Grant No. 2023YFB3811400), National Natural Science Foundation of China (No. 52273296 and No. 51872154), Beijing Municipal Science & Technology Commission (No. Z221100006722016).

M. Wu and Q. Z. carried out the theoretical analysis and wrote the manuscript. M. W. and M. Wu performed the experiments and simulations. All authors contributed to the final version of the manuscript.

*These authors contributed equally to this work.
†zhaoqian@tsinghua.edu.cn

[1] N. P. Armitage, E. J. Mele, and A. Vishwanath, Rev. Mod. Phys. **90**, 015001 (2018).
[2] X. Wan, A. M. Turner, A. Vishwanath, and S. Y. Savrasov, Phys. Rev. B **83**, 205101 (2011).
[3] P. Hosur and X. Qi, C.R. Phys. **14**, 857 (2013), topological insulators / Isolants topologiques.
[4] A. A. Burkovj, J. Phys. Condens. Matter **27**, 113201 (2015).
[5] Q. Wu, A. A. Soluyanov, and T. Bzdušek, Science **365**, 1273 (2019).
[6] A. A. Burkov, M. D. Hook, and L. Balents, Phys. Rev. B **84**, 235126 (2011).
[7] C. Fang, H. Weng, X. Dai, and Z. Fang, Chin. Phys. B **25**, 117106 (2016).
[8] W. Gao, B. Yang, B. Tremain, H. Liu, Q. Guo, L. Xia, A. P. Hibbins, and S. Zhang, Nat. Commun. **9**, 950 (2018).
[9] L. Xia, Q. Guo, B. Yang, J. Han, C.-X. Liu, W. Zhang, and S. Zhang, Phys. Rev. Lett. **122**, 103903 (2019).
[10] T. Bzdušek, Q. Wu, A. Rüegg, M. Sigrist, and A. A. Soluyanov, Nature (London) **538**, 75 (2016).
[11] Q. Yan, R. Liu, Z. Yan, B. Liu, H. Chen, Z. Wang, and L. Lu, Nat. Phys. **14**, 461 (2018).
[12] Z. Yang, C.-K. Chiu, C. Fang, and J. Hu, Phys. Rev. Lett. **124**, 186402 (2020).
[13] H. Kedia, I. Bialynicki-Birula, D. Peralta-Salas, and W. T. M. Irvine, Phys. Rev. Lett. **111**, 150404 (2013).
[14] R. Bi, Z. Yan, L. Lu, and Z. Wang, Phys. Rev. B **96**, 201305 (2017).
[15] C. H. Lee, A. Sutrisno, T. Hofmann, T. Helbig, Y. Liu, Y. S. Ang, L. K. Ang, X. Zhang, M. Greiter, and R. Thomale, Nat. Commun. **11**, 4385 (2020).
[16] Z. Yan, R. Bi, H. Shen, L. Lu, S.-C. Zhang, and Z. Wang, Phys. Rev. B **96**, 041103 (2017).
[17] Y. Xie, J. Cai, J. Kim, P.-Y. Chang, and Y. Chen, Phys. Rev. B **99**, 165147 (2019).
[18] F. N. Ünal, A. Bouhon, and R.-J. Slager, Phys. Rev. Lett. **125**, 053601 (2020).
[19] E. Yang, B. Yang, O. You, H.-C. Chan, P. Mao, Q. Guo, S. Ma, L. Xia, D. Fan, Y. Xiang, and S. Zhang, Phys. Rev. Lett. **125**, 033901 (2020).
[20] M. Z. Hasan, S.-Y. Xu, and G. Bian, Phys. Scr. **2015**, 014001 (2015).
[21] R. Yu, Q. Wu, Z. Fang, and H. Weng, Phys. Rev. Lett. **119**, 036401 (2017).

[22] R. Yu, H. Weng, Z. Fang, X. Dai, and X. Hu, Phys. Rev. Lett. **115**, 036807 (2015).
[23] Z. Yan and Z. Wang, Phys. Rev. Lett. **117**, 087402 (2016).
[24] C. Gong, Y. Xie, Y. Chen, H.-S. Kim, and D. Vanderbilt, Phys. Rev. Lett. **120**, 106403 (2018).
[25] S.-S. Wang, Y. Liu, Z.-M. Yu, X.-L. Sheng, and S. A. Yang, Nat. Commun. **8**, 1844 (2017).
[26] H. Park, W. Gao, X. Zhang, and S. S. Oh, Nanophotonics **11**, 2779 (2022).
[27] T. Bzdušek and M. Sigrist, Phys. Rev. B **96**, 155105 (2017).
[28] X.-Q. Sun, S.-C. Zhang, and T. Bzdušek, Phys. Rev. Lett. **121**, 106402 (2018).
[29] A. Tiwari and T. Bzdušek, Phys. Rev. B **101**, 195130 (2020).
[30] A. Bouhon, Q. Wu, R.-J. Slager, H. Weng, O. V. Yazyev, and T. Bzdušek, Nat. Phys. **16**, 1137 (2020).
[31] M. Wang, S. Liu, Q. Ma, R.-Y. Zhang, D. Wang, Q. Guo, B. Yang, M. Ke, Z. Liu, and C. T. Chan, Phys. Rev. Lett. **128**, 246601 (2022).
[32] H. Park, S. Wong, A. Bouhon, R.-J. Slager, and S. S. Oh, Phys. Rev. B **105**, 214108 (2022).
[33] B. Jiang, A. Bouhon, Z.-K. Lin, X. Zhou, B. Hou, F. Li, R.-J. Slager, and J.-H. Jiang, Nat. Phys. **17**, 1239 (2021).
[34] Q. Guo, T. Jiang, R.-Y. Zhang, L. Zhang, Z.-Q. Zhang, B. Yang, S. Zhang, and C. T. Chan, Nature (London) **594**, 195 (2021).
[35] R.-J. Slager, A. Bouhon, and F. N. Ünal, arXiv:2208.12824.
[36] S. Chen, A. Bouhon, R.-J. Slager, and B. Monserrat, Phys. Rev. B **105**, L081117 (2022).
[37] B. Peng, A. Bouhon, R.-J. Slager, and B. Monserrat, Phys. Rev. B **105**, 085115 (2022).
[38] G. Bian, T.-R. Chang, H. Zheng, S. Velury, S.-Y. Xu, T. Neupert, C.-K. Chiu, S.-M. Huang, D. S. Sanchez, I. Belopolski, N. Alidoust, P.-J. Chen, G. Chang, A. Bansil, H.-T. Jeng, H. Lin, and M. Z. Hasan, Phys. Rev. B **93**, 121113 (2016).
[39] G. Bian, T.-R. Chang, R. Sankar, S.-Y. Xu, H. Zheng, T. Neupert, C.-K. Chiu, S.-M. Huang, G. Chang, I. Belopolski *et al.*, Nat. Commun. **7**, 10556 (2016).
[40] Z. Liu, L. Yang, Y. Sun, T. Zhang, H. Peng, H. Yang, C. Chen, Y. f. Zhang, Y. Guo, D. Prabhakaran *et al.*, Nat. Mater. **15**, 27 (2016).
[41] B. Yang, Q. Guo, B. Tremain, R. Liu, L. E. Barr, Q. Yan, W. Gao, H. Liu, Y. Xiang, J. Chen *et al.*, Science **359**, 1013 (2018).
[42] C. Fang, Y. Chen, H.-Y. Kee, and L. Fu, Phys. Rev. B **92**, 081201 (2015).
[43] M. Z. Hasan and C. L. Kane, Rev. Mod. Phys. **82**, 3045 (2010).
[44] L. Lu, Nat. Phys. **14**, 875 (2018).
[45] C. H. Lee, S. Imhof, C. Berger, F. Bayer, J. Brehm, L. W. Molenkamp, T. Kiessling, and R. Thomale, Communi. Phys. **1**, 1 (2018).
[46] T. Helbig, T. Hofmann, S. Imhof, M. Abdelghany, T. Kiessling, L. Molenkamp, C. Lee, A. Szameit, M. Greiter, and R. Thomale, Nat. Phys. **16**, 747 (2020).
[47] J. Ningyuan, C. Owens, A. Sommer, D. Schuster, and J. Simon, Phys. Rev. X **5**, 021031 (2015).
[48] S. Imhof, C. Berger, F. Bayer, J. Brehm, L. W. Molenkamp, T. Kiessling, F. Schindler, C. H. Lee, M. Greiter, T. Neupert *et al.*, Nat. Phys. **14**, 925 (2018).
[49] W. Zhang, D. Zou, Q. Pei, W. He, J. Bao, H. Sun, and X. Zhang, Phys. Rev. Lett. **126**, 146802 (2021).
[50] See Supplemental Material at http://link.aps.org/supplemental/10.1103/PhysRevLett.132.016605 for details about (1) momentum-resolved circuits, (2) CP stability, (3) non-Abelian *CP* entangling, (4) emergent symmetry, and (5) experimental details. It includes Refs. [51–53].
[51] Y. V. Fyodorov, in *2016 URSI International Symposium on Electromagnetic Theory (EMTS), Espoo, Finalnd* (IEEE, 2016), pp. 666–669.
[52] J. Barthélemy, O. Legrand, and F. Mortessagne, Phys. Rev. E **71**, 016205 (2005).
[53] T. Helbig, T. Hofmann, C. H. Lee, R. Thomale, S. Imhof, L. W. Molenkamp, and T. Kiessling, Phys. Rev. B **99**, 161114 (2019).
[54] M. Wu, Q. Zhao, L. Kang, M. Weng, Z. Chi, R. Peng, J. Liu, D. H. Werner, Y. Meng, and J. Zhou, Phys. Rev. B **107**, 064307 (2023).
[55] Y. V. Fyodorov and H.-J. Sommers, J. Math. Phys. (N.Y.) **38**, 1918 (1997).
[56] F.-M. Dittes, Phys. Rep. **339**, 215 (2000).
[57] Here, we focus on the homotopic degeneracy conversions, the effects caused by the conversions, like the Fermi arc and parallel transport, may be a little out of the scope of the paper, so we use LTspice simulation to observe them.
[58] A. Nelson, T. Neupert, A. Alexandradinata, and T. c. v. Bzdušek, Phys. Rev. B **106**, 075124 (2022).
[59] Z. Yang, F. Gao, X. Shi, X. Lin, Z. Gao, Y. Chong, and B. Zhang, Phys. Rev. Lett. **114**, 114301 (2015).
[60] Q. Zhao, J. Zhou, F. Zhang, and D. Lippens, Mater. Today **12**, 60 (2009).